Three-axis Motion Compensated Crane Head Control ⋆

Vegard Wie Henriksen * **Audun Gerhardsen Røine** *
Espen Skjong *,**,⋆⋆ **Tor Arne Johansen** *

* *Centre for Autonomous Marine Operations and Systems, Department of Engineering Cybernetics, Norwegian University of Science and Technology, Trondheim, Norway.*
** *Ulstein Power & Control AS, Norway.*

Abstract: Offshore operations can be harsh and demanding and set personnel and equipment at risk. Ships will be exposed to the elemental forces of wind, waves and current, which will influence offshore crane operations considerably. This paper addresses the use of a crane head, constructed as a Delta parallel robot, to compensate for the motions of the ship in three axes. This type of robot has a rigid and accurate structure, but because of its highly nonlinear nature, advanced control algorithms must be derived. This paper includes both forward and inverse kinematics for the robot, as well as velocity kinematics and workspace analysis. The kinematics of a full crane system, with the robot as its head, has been modelled, and a simulator which includes a model of a supply vessel is created. The disturbances on the system from the elements are translated and rotated to the crane head frame of reference for use in the compensation procedure. PID controllers are used to control the crane head, and simulations are conducted to verify that the crane head is able to compensate for the motions created by waves.

Keywords: Motion compensation, Nonlinear control, Robotics, Ship dynamics, Cranes

1. INTRODUCTION

Offshore crane operations in harsh environments are challenging and put crew and equipment at risk. Heave compensated crane systems in marine vessels have been extensively used to cultivate easier and safer offshore operations. Examples of such operations are surface crane operations for installing equipment on the seafloor, launching and retrieving systems (LARS) and delivering supplies from vessels to platforms. Motion compensation in such systems are generally limited to one axis, i.e the vertical heave motion, (Fang et al., 2014; Küchler et al., 2011; Messineo and Serrano, 2009; Johansen et al., 2003).

This paper considers the development of a crane head control designed for motion compensation in all three axes. This Three Axis Compensator (TAC) is a Delta type parallel robot (Clavel, 1988). A parallel robot consists of two or more closed kinematic chains linking the base to the end effector, whereas a serial robot arm consists of just one kinematic chain (Spong et al., 2005). The advantages of a parallel structure are its high rigidity and accuracy, making it very attractive for crane operations, whereas the disadvantages are narrower workspace and more difficult control than its serial counterpart (Laribi et al., 2008). The Delta robot consists of three kinematic chains connected on either end at a top- and bottom plate, and these plates stay in parallel with each other (Codourey, 1988). It is most commonly used for precise and stationary actions such as item picking or 3D printing (Williams, 2015), but in this paper it will be seen that it can also be used for motion compensation of crane operations on ships, which is a novel application.

It will be discussed how to use the TAC to compensate for the motion of a load suspended in a crane on a ship at sea. First a mathematical model of the crane head will be provided. Section 2 deduces the crane head geometry which is used in Sections 3, 4 and 5 to find the inverse, forward and velocity kinematics of the TAC, respectively. The workspace limits of the TAC are explored in Section 6. The kinematics of the full crane system, including how the measurements from the Inertial Measurement Unit (IMU) are related to the states of the system is detailed in Section 7, whereas Section 8 will tie together all the different parts required to control the TAC. The simulation setup and results are presented in Sections 9 and 10.

2. TAC GEOMETRY

To fully understand how the TAC can be used for motion compensation, it is imperative that the TAC's configuration can be explained and designed precisely. Fig. 1 shows a geometrical representation of the TAC with the different parameters further explained in Table 1. The Tool Center Point (TCP) is where the load is suspended, and its position is denoted $\mathbf{p}_c$.

The main frame of orientation, denoted $\{t\}$ with coordinates (x_t, y_t, z_t), is shown in Fig. 2, with the x-axis

⋆ This work has been carried out at the Centre for Autonomous Marine Operations and Systems (NTNU AMOS). The Norwegian Research Council is acknowledged as the main sponsor of NTNU AMOS. This work was supported by Ulstein Power & Control AS and the Research Council of Norway, Project number 241205.
⋆⋆Corresponding author: espen.skjong@ulstein.com

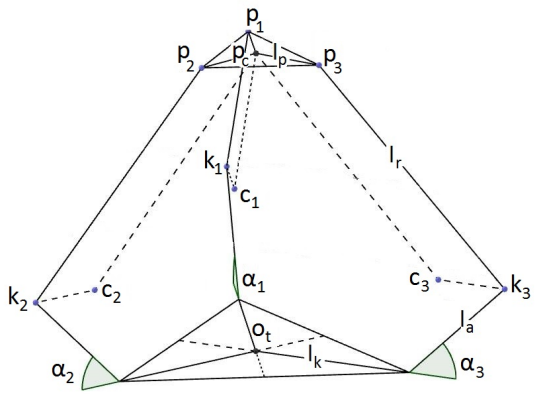

Fig. 1. TAC Geometry.

Table 1. TAC parameters.

Notation	Unit	Description
l_k	m	Length from center of the bottom plate to the arm
l_a	m	Length of the arm
l_r	m	Length of the rod
l_p	m	Length from the center of the top plate to the rod
α_i	rad	Angle between bottom plate and arm i
u_i	rad	input to DC-motors
$\mathbf{k}_i$	-	Knee-point between arm and rod i
$\mathbf{c}_i$	-	Indented Knee-point i
$\mathbf{p}_i$	-	Point connecting rod and top plate
$\mathbf{p}_c$	-	Center-point of the top plate, position of the TCP
i	-	Jointed-arm number, $i \in \{1, 2, 3\}$.

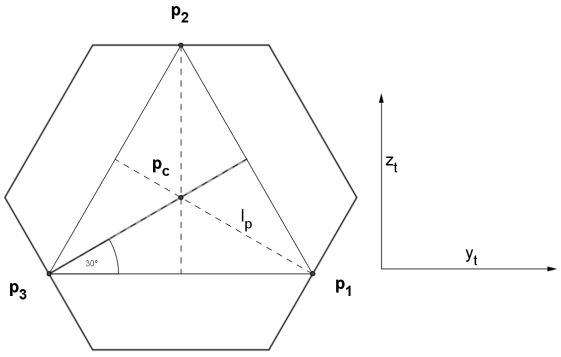

Fig. 2. TAC top plate seen from above, frame $\{t\}$.

pointing out of the paper plane, z-axis up and the y-axis to the right. In Fig. 3 the individual frame for any joint is shown, denoted $\{t_i\}= (x_{t_i}, y_{t_i}, z_{t_i})$ for $i \in \{1, 2, 3\}$, where the y-axis points from the knee into the center. Both $\{t\}$- and $\{t_i\}$-frame have the same origin, $\mathbf{o}_t$, thus transforming between these frames is done by rotations, with the rotation matrices

$$\mathbf{R}^t_{t_1} = \mathbf{R}_{x,\frac{5\pi}{6}}, \quad \mathbf{R}^t_{t_2} = \mathbf{R}_{x,\frac{3\pi}{2}}, \quad \mathbf{R}^t_{t_3} = \mathbf{R}_{x,\frac{\pi}{6}}. \tag{1}$$

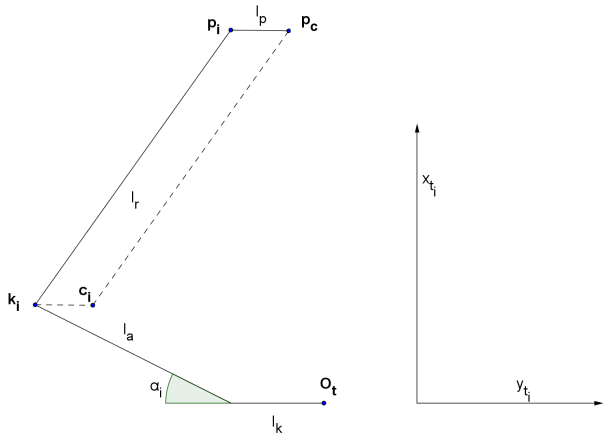

Fig. 3. TAC arm i seen from one of the sides, frame $\{t_i\}$.

The position of the TCP in the different frames is denoted as

$$\mathbf{p}^t_c = [x_c \;\; y_c \;\; z_c]^T \text{ and } \mathbf{p}^{t_i}_c = (\mathbf{R}^t_{t_i})^T \mathbf{p}^t_c = [x_{ci} \quad y_{ci} \quad z_{ci}]^T. \tag{2}$$

Each of the three kinematic chains consists of an arm and a rod, connected by a knee joint. The position of the knee, $\mathbf{k}_i$, can be derived, when knowing the corresponding angle α_i, as

$$\mathbf{k}^t_i = \mathbf{R}^t_{t_i} [l_a \cos\alpha_i, \; -l_k - l_a \sin\alpha_i, \; 0]^T \quad \forall i \in \{1, 2, 3\}, \tag{3}$$

whereas the position of the top plate cannot be found without knowing all three angles. The length of the rod, l_r, is constant, a fact that can be exploited to derive the relation between all angles and the TCP. By placing an indented knee-point, $\mathbf{c}_i$, a distance of l_p in the y_{t_i}-direction in the $\{t_i\}$-frame yields a point which will be at a constant distance of l_r from $\mathbf{p}_c$. $\mathbf{c}_i$ can be described as

$$\mathbf{c}^t_i = \mathbf{R}^t_{t_i} [l_a \sin\alpha_i, \quad a - l_a \cos\alpha_i, \quad 0]^T, \quad \forall i \in \{1, 2, 3\}, \tag{4}$$

where $a = l_p - l_k$. The vector $\mathbf{s}^t_i$ is defined as the vector from $\mathbf{c}^t_i$ to $\mathbf{p}^t_c$, i.e.

$$\mathbf{s}^t_i \equiv \mathbf{p}^t_c - \mathbf{c}^t_i \quad \forall i \in \{1, 2, 3\}. \tag{5}$$

$\boldsymbol{p}^t_c$ can be seen as the crossing point of three spheres with radius l_r and center in each indented knee point $\boldsymbol{c}^t_i$, as presented in Fig. 4. With this information, the vector-loop closure equation can be found as

$$\|\mathbf{s}^t_i\|^2_2 = l^2_r \quad \forall i \in \{1, 2, 3\}, \tag{6}$$

Eq. (6) is a useful tool for describing the system dynamics (Codourey (1988); Williams (2015); Andrioaia et al. (2012)).

3. INVERSE POSITION KINEMATICS

The Inverse Position Kinematics (IPK) solution of the system is a way of finding the joint angles, $\boldsymbol{\alpha} = [\alpha_1 \;\; \alpha_2 \;\; \alpha_3]^T$, given the Cartesian coordinates of the TCP, $\mathbf{p}^t_c$ (Williams, 2015). This is done in the $\{t_i\}$-frame, where

$$\mathbf{c}^{t_i}_i = [x_i \quad y_i \quad z_i]^T. \tag{7}$$

Eq. (6) can be expanded,

$$\|\mathbf{p}^{t_i}_c\|^2_2 + \|\mathbf{c}^{t_i}_i\|^2_2 - l^2_r - 2(x_{ci}x_i + y_{ci}y_i + z_{ci}z_i) = 0, \tag{8}$$

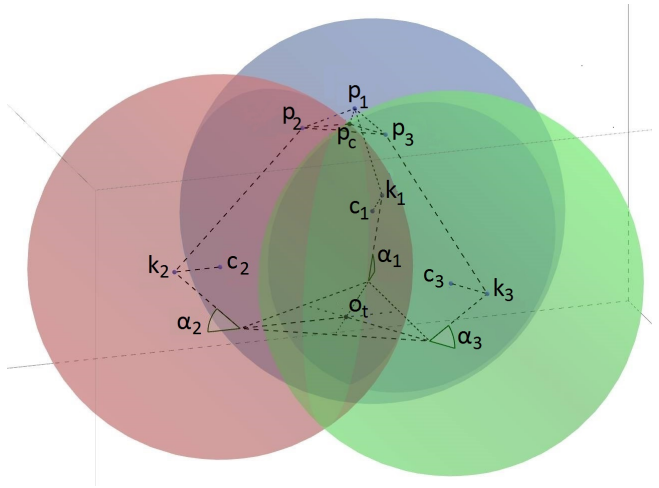

Fig. 4. Tool Center Point $\boldsymbol{p}_c^t$ described by three spheres.

where

$$\|\mathbf{c}_i^{t_i}\|_2^2 = l_a^2 + a^2 - 2al_a\cos\alpha_i. \tag{9}$$

Eq. (8) is then expanded for all three joints in the individual $\{t_i\}$-frames

$$\begin{aligned}
&\|\mathbf{p}_c^{t_1}\|_2^2 + \|\mathbf{c}_1^{t_1}\|_2^2 - l_r^2 - 2x_{c1}l_a\sin\alpha_1 \\
&\quad + (\sqrt{3}y_{c1} - z_{c1})(a - l_a\cos\alpha_1) = 0, \\
&\|\mathbf{p}_c^{t_2}\|_2^2 + \|\mathbf{c}_2^{t_2}\|_2^2 - l_r^2 - 2x_{c2}l_a\sin\alpha_2 \\
&\quad + 2z_{c2}(a - l_a\cos\alpha_2) = 0, \\
&\|\mathbf{p}_c^{t_3}\|_2^2 + \|\mathbf{c}_3^{t_3}\|_2^2 - l_r^2 - 2x_{c3}l_a\sin\alpha_3 \\
&\quad - (\sqrt{3}y_{c3} + z_{c3})(a - l_a\cos\alpha_3) = 0,
\end{aligned} \tag{10}$$

where the three equations are of the form

$$e_i\cos\alpha_i + f_i\sin\alpha_i + g_i = 0 \quad \forall i \in \{1,2,3\}, \tag{11}$$

with

$$\begin{aligned}
f_1 &= f_2 = f_3 = -2x_{ci}l_a, \\
e_1 &= (-\sqrt{3}y_{c1} + z_{c1} - 2a)l_a, \\
e_2 &= -2(z_{c2} + a)l_a, \\
e_3 &= (\sqrt{3}y_{c3} + z_{c3} + 2a)l_a, \\
g_1 &= \|\mathbf{p}_c^{t_1}\|_2^2 + l_a^2 + a^2 - l_r^2 + (\sqrt{3}y_{c1} - z_{c1})a, \\
g_2 &= \|\mathbf{p}_c^{t_2}\|_2^2 + l_a^2 + a^2 - l_r^2 + 2z_{c2}a, \\
g_3 &= \|\mathbf{p}_c^{t_3}\|_2^2 + l_a^2 + a^2 - l_r^2 - (\sqrt{3}y_{c3} + z_{c3})a.
\end{aligned} \tag{12}$$

Tangent Half-Angle Substitution (Williams, 2015) is a method that can be used to solve (11). By defining a variable $\gamma_i \equiv \tan(\frac{\alpha_i}{2})$, $\cos\alpha_i$ and $\sin\alpha_i$ can be substituted with

$$\cos\alpha_i = \frac{1-\gamma_i^2}{1+\gamma_i^2}, \quad \sin\alpha_i = \frac{2\gamma_i}{1+\gamma_i^2}. \tag{13}$$

Inserting (13) into (11) leads to

$$(g_i - e_i)\gamma_i^2 + (2f_i)\gamma_i + (g_i + e_i) = 0. \tag{14}$$

One can recognize (14) as a second order polynomial which can be solved with the quadratic formula

$$\gamma_{i_{1,2}} = \frac{-f_i \pm \sqrt{e_i^2 + f_i^2 - g_i^2}}{g_i - e_i} \tag{15}$$

This yields two solutions for γ_i, and two solutions for α_i since $\alpha_i = 2\arctan(\gamma_i)$. One solution has the knees pointing outwards, $\alpha_i < \pi/2$ and the other has the knees pointing inwards, $\alpha_i > \pi/2$. As long as the TCP is inside the workspace, the solutions are well-defined and real. When the solutions are different this will in total yield eight different configurations for the TAC, but the solution chosen should be the one with all knees pointing outward, i.e. satisfying $|\alpha_i| < \frac{\pi}{2}$. The IPK solution can be formed into a function such that

$$\boldsymbol{\alpha} = IPK(\mathbf{p}_c^t). \tag{16}$$

4. FORWARD POSITION KINEMATICS

The Forward Position Kinematics (FPK) solution is the inverse of the IPK as it yields $\mathbf{p}_c^t$ given $\boldsymbol{\alpha}$. It can be solved analytically with Gaussian Elimination (Coope, 2000). Eq. (6) can be rewritten as

$$(\boldsymbol{p}_c^t)^T\boldsymbol{p}_c^t - 2(\boldsymbol{p}_c^t)^T\boldsymbol{c}_i^t + (\boldsymbol{c}_i^t)^T\boldsymbol{c}_i^t = l_r^2. \tag{17}$$

One want to reformulate the quadratic parts of the equation to make it easier to solve. This can be done by introducing the variables

$$r = (\boldsymbol{p}_c^t)^T\boldsymbol{p}_c^t, \quad b_i = (\boldsymbol{c}_i^t)^T\boldsymbol{c}_i^t - l_r^2, \tag{18}$$

which gives

$$(\mathbf{p}_c^t)^T\mathbf{c}_i^t = (r + b_i)/2, \quad \forall i \in \{1,2,3\}. \tag{19}$$

By changing the notation to

$$\mathbf{C} = \begin{bmatrix}\mathbf{c}_1^t & \mathbf{c}_2^t & \mathbf{c}_3^t\end{bmatrix}, \quad \mathbf{1} = [1\ 1\ 1]^T, \quad \mathbf{b} = [b_1\ b_2\ b_3]^T, \tag{20}$$

and introduce the substitution variables

$$\mathbf{u} = \mathbf{C}^{-T}\mathbf{1}, \quad \mathbf{v} = \mathbf{C}^{-T}\mathbf{b}, \tag{21}$$

a solution for $\boldsymbol{p}_c^t$ can be found as

$$\boldsymbol{p}_c^t = (r\mathbf{u} + \mathbf{v})/2. \tag{22}$$

A solution for $\boldsymbol{p}_c^t$ is now presented, but r is still unknown. r can be obtained by inserting (22) into (18)

$$r = (\boldsymbol{p}_c^t)^T\boldsymbol{p}_c^t = \frac{1}{4}(r\mathbf{u} + \mathbf{v})^T(r\mathbf{u} + \mathbf{v}). \tag{23}$$

This can again be rewritten to

$$(\mathbf{u}^T\mathbf{u})r^2 + (2\mathbf{u}^T\mathbf{v} - 4)r + \mathbf{v}^T\mathbf{v} = 0, \tag{24}$$

which can be recognized as a second order polynomial. This can be solved for r as

$$r = \frac{2 - \mathbf{u}^T\mathbf{v} \pm \sqrt{(2 - \mathbf{u}^T\mathbf{v})^2 - (\mathbf{u}^T\mathbf{u})(\mathbf{v}^T\mathbf{v})}}{\mathbf{u}^T\mathbf{u}} \tag{25}$$

If the solution from (25) is inserted in (22) two analytical solution for $\boldsymbol{p}_c^t$ given $\boldsymbol{\alpha}$ appears. To understand why two solutions appears one can look back at Fig. 4 where it can be observed that the three spheres intersect in two points. One solution is the intersection above the TAC base plate, the other is beneath. The valid solution for the crane head is the one over the TAC base plate i.e satisfying $x_c^t > x_i^t$ $\forall i \in \{1,2,3\}$.

5. KINEMATIC JACOBIAN

The relationship between the velocity of the TCP, $\dot{\mathbf{p}}_c$, and the joint velocities, $\dot{\boldsymbol{\alpha}}$, can be useful for designing a control system (Codourey (1988); Spong et al. (2005)). This kinematic relationship can be found by differentiating (6) as

$$(\mathbf{s}_i^t)^T\dot{\mathbf{s}}_i^t = 0 \tag{26}$$

where $\dot{\mathbf{s}}_i$ can be found as

$$\dot{\mathbf{s}}_i^t = \dot{\mathbf{p}}_c^t - \mathbf{d}_i^t\dot{\alpha}_i, \tag{27}$$

with

$$\mathbf{d}_i^t = \mathbf{R}_{t_i}^t \left[l_a \cos\alpha_i \;\; l_a \sin\alpha_i \;\; 0 \right]^T. \tag{28}$$

Inserting (26) into (27) yields

$$(\mathbf{s}_i^t)^T(\dot{\mathbf{p}}_c^t - \mathbf{d}_i^t\dot{\alpha}_i) = 0. \tag{29}$$

Expanding (29) for $i \in \{1,2,3\}$ gives

$$\begin{bmatrix} (\mathbf{s}_1^t)^T \\ (\mathbf{s}_2^t)^T \\ (\mathbf{s}_3^t)^T \end{bmatrix} \dot{\mathbf{p}}_c - \begin{bmatrix} (\mathbf{s}_1^t)^T\mathbf{d}_1^t & 0 & 0 \\ 0 & (\mathbf{s}_2^t)^T\mathbf{d}_2^t & 0 \\ 0 & 0 & (\mathbf{s}_3^t)^T\mathbf{d}_3^t \end{bmatrix} \dot{\boldsymbol{\alpha}} = 0, \tag{30}$$

which finally becomes

$$\dot{\mathbf{p}}_c^t = \mathbf{J}(\mathbf{p}_c^t, \boldsymbol{\alpha})\dot{\boldsymbol{\alpha}}, \tag{31}$$

where

$$\mathbf{J}(\mathbf{p}_c^t, \boldsymbol{\alpha}) = \begin{bmatrix} (\mathbf{s}_1^t)^T \\ (\mathbf{s}_2^t)^T \\ (\mathbf{s}_3^t)^T \end{bmatrix}^{-1} \begin{bmatrix} (\mathbf{s}_1^t)^T\mathbf{d}_1^t & 0 & 0 \\ 0 & (\mathbf{s}_2^t)^T\mathbf{d}_2^t & 0 \\ 0 & 0 & (\mathbf{s}_3^t)^T\mathbf{d}_3^t \end{bmatrix} \tag{32}$$

is the Jacobian of the system.

6. WORKSPACE

The IPK solution described in Section 3 will meet difficulties if the position is outside the reachable area of the TAC, i.e. the workspace. To this end, a check to see if the desired position is inside the workspace is necessary. Since the TAC is to be used for motion compensation, it is imperative that it is reliable. If a desired position is found to be outside of the workspace, additional crane joints (if available) must be utilized, operations must be aborted, or reduced accuracy of the motion compensation must be accepted. A method for finding the workspace can be found with the help of Andrioaia et al. (2012). It is possible to design a TAC based on workspace requirements (Stan et al., 2011) but this will not be treated in this paper.

The first step in finding the workspace is to make a cube containing the limits of the maximum reach of the TCP. The approximated limits stay true to the notion that the top plate can not go through the bottom plate, nor that it can be flipped. Hence, the limits are found to be

$$\begin{aligned} X_{max} &= l_a + l_r \\ X_{min} &= 0 \\ Y_{max} &\cong Z_{max} = l_r + l_p - l_k \\ Y_{min} &\cong Z_{min} = -(l_r + l_p - l_k). \end{aligned} \tag{33}$$

The limits can be combined to form the intervals that contain both feasible and infeasible solutions for $\mathbf{p}_c^t$. These intervals are then split into individual points in three dimensions that can be tested as candidate positions for the TCP. The number of points selected will depend on the spatial discretization distance h, which acts as the distance between points in one dimensions. This yields the arrays

$$\begin{aligned} \mathbf{x_w} &= [x_{w1}, x_{w2}, ..., x_{wn}] \\ \mathbf{y_w} &= [y_{w1}, y_{w2}, ..., y_{wn}] \\ \mathbf{z_w} &= [z_{w1}, z_{w2}, ..., z_{wn}] \end{aligned} \tag{34}$$

where $x_{w1} = X_{min}$, $x_{wn} = X_{max}$, $y_{w1} = Y_{min}$, $y_{wn} = Y_{max}$, $z_{w1} = Z_{min}$ and $z_{wn} = Z_{max}$ with fixed step size h. All the different positions found in these arrays are then checked by testing if the IPK solution is real, and joint angles are inside the design range. The positions that are deemed plausible are kept and serves as the basis for the approximated workspace. The smaller h, the higher the resolution of the workspace and the cost of computational load. The plausible coordinates on the outskirts of the workspace will serve as the edges, and by finding the convex hull of all the allowed coordinates, the limits of the workspace is found. With the limits found, it is possible to check if the desired position is outside the limits while the TAC is running. Appropriate actions for transgressing the limits can be moving the set point back towards the limits (saturation), involving the rest of the crane in the compensation action, or aborting the operation, among other alternatives. This paper will not consider the actions for transgressing the limits further. As it is a cumbersome process to find the limits it should be done as an initializing process, or even done separately and merely entering the limits as parameters to the TAC's controller.

7. FULL CRANE KINEMATICS

This section will describe the forward and velocity kinematics of a full crane system, from the Center of Origin (CO) to the TAC. Two more coordinate reference frames are described. The North-East-Down (NED) coordinate system, $\{\text{n}\} = (x_n, y_n, z_n)$ with origin $\mathbf{o}_n$, is defined relative to the Earth's reference ellipsoid, and stays fixed as the ship moves. The body-fixed reference frame, $\{\text{b}\} = (x_b, y_b, z_b)$ with origin $\mathbf{o}_b$ (CO), is a moving coordinate frame that is fixed to the craft (Fossen, 2011).

Table 2. Notation for marine vessels (SNAME, 1950).

DOF		**Linear and angular velocities**	**Positions and Euler angles**
1	motions x dir (surge)	u	x
2	motions y dir (sway)	v	y
3	motions z dir (heave)	w	z
4	rotation x axis (roll)	p	ϕ
5	rotation y axis (pitch)	q	θ
6	rotation z axis (yaw)	r	ψ

Marine vessels are affected by forces and moments in six Degrees Of Freedom (DOF), which are further described in Table 2. The IMU normally consists of accelerometers and gyroscopes, among other sensors, used to estimate the ship's position and attitude, and the velocities of these, as

$$\begin{aligned} \boldsymbol{\eta} &= [x \;\; y \;\; z \;\; \phi \;\; \theta \;\; \psi]^T, \\ \boldsymbol{\nu} &= [u \;\; v \;\; w \;\; p \;\; q \;\; r]^T. \end{aligned} \tag{35}$$

The IMU measures accelerations, which are integrated to get velocities $\boldsymbol{\nu}$ and position $\boldsymbol{\eta}$. Sensor biases, misalignments and noise will cause drift, especially in the position estimations. To obtain measurements of higher quality the IMU has to be combined with other systems. Combining the IMU with the kinematic equations for the ship results in an inertial navigation system (INS), but the measurements still drifts. By including Global Navigation Satellite System (GNSS) measurements in the computations, the INS drift can be removed. Obviously the acceleration measurement quality depends on the IMU quality while the velocity and position measurement quality depends on the GNSS quality (Fossen, 2011).

The transformation from {b}-frame to {n}-frame can be found as

Table 3. DH table for a typical crane configuration.

Link	$\boldsymbol{a}_j$	$\boldsymbol{\alpha}_j$	$\boldsymbol{d}_j$	$\boldsymbol{\theta}_j$
1	L_{sx}	π	$-L_{sz}$	0
2	0	$\frac{\pi}{2}$	L_0	β_0^*
3	L_1	0	0	β_1^*
4	L_2	$-\frac{\pi}{2}$	0	β_2^*

$$\boldsymbol{T}_b^n = \begin{bmatrix} \boldsymbol{R}_b^n & \boldsymbol{o}_b^n \\ \boldsymbol{0} & 1 \end{bmatrix}, \tag{36}$$

where

$$\begin{aligned} \boldsymbol{R}_b^n &= \boldsymbol{R}_{x,\phi}\boldsymbol{R}_{y,\theta}\boldsymbol{R}_{z,\psi}, \\ \boldsymbol{o}_b^n &= [x \ y \ z]^T. \end{aligned} \tag{37}$$

The forward kinematics of the full crane system can be found by using the DH-convention, with the knowledge of the crane's dimensions and configuration (Spong et al., 2005). The following example, seen in Fig. 5, is considering the transformation from $\boldsymbol{o}_b$ inside the ship, along a three-joint crane system to $\boldsymbol{o}_t$. With the information available in Fig. 5, a DH-table can be made, see Table 3. β_j^* are controllable angles. Each row in the DH-table is inserted into (38) to garner the transformation matrix A_j from link $j-1$ to link j, and in this example $j = 1, 2, 3, 4$.

$$\begin{aligned} \boldsymbol{A}_j &= \boldsymbol{Rot}_{z,\theta_j}\boldsymbol{Trans}_{z,d_j}\boldsymbol{Trans}_{x,a_j}\boldsymbol{Rot}_{z,\alpha} \\ &= \begin{bmatrix} c_{\theta_j} & -s_{\theta_j}c_{\alpha_j} & s_{\theta_j}s_{\alpha_j} & a_j c_{\theta_j} \\ s_{\theta_j} & c_{\theta_j}c_{\alpha_j} & -c_{\theta_j}s_{\alpha_j} & a_j s_{\theta_j} \\ 0 & s_{\alpha_j} & c_{\alpha_j} & d_j \\ 0 & 0 & 0 & 1 \end{bmatrix} \end{aligned} \tag{38}$$

The notation for $\sin(\cdot)$ and $\cos(\cdot)$ in (38) is $s_x \equiv \sin x$ and $c_x \equiv \cos x$. The transformation matrix between frames can be found as

$$\mathbf{T}_n^0 = \mathbf{A}_0 \cdots \mathbf{A}_n \tag{39}$$

where n is the number of joints. The transformation matrix can be further broken down as

$$\mathbf{T}_n^0 = \begin{bmatrix} \boldsymbol{R}_n^0 & \boldsymbol{o}_n^0 \\ \boldsymbol{0} & 1 \end{bmatrix} = \begin{bmatrix} \boldsymbol{x}_n^0 & \boldsymbol{y}_n^0 & \boldsymbol{z}_n^0 & \boldsymbol{o}_n^0 \\ 0 & 0 & 0 & 1 \end{bmatrix}, \tag{40}$$

where $\boldsymbol{R}_n^0$ is a rotation matrix consisting of the three vectors $\boldsymbol{x}_n^0$, $\boldsymbol{y}_n^0$ and $\boldsymbol{z}_n^0$, and $\boldsymbol{o}_n^0$ is the translation vector.

$$\boldsymbol{T}_t^b = \boldsymbol{T}_4^1 = \boldsymbol{A}_1\boldsymbol{A}_2\boldsymbol{A}_3\boldsymbol{A}_4 = \begin{bmatrix} \boldsymbol{R}_t^b & \boldsymbol{o}_t^b \\ \boldsymbol{0} & 1 \end{bmatrix}. \tag{41}$$

The inverse kinematics for the full crane is the method of finding the joint angles, $\boldsymbol{\beta}$, knowing the position of the end-effector, $\boldsymbol{o}_t^b$. By transforming this to the position of the first joint, $\boldsymbol{o}_t^0$ can be found as

$$\boldsymbol{o}_t^0 = \boldsymbol{R}_b^0\boldsymbol{o}_t^b + \boldsymbol{o}_b^0 = \begin{bmatrix} x_b^0 & y_b^0 & z_b^0 \end{bmatrix}. \tag{42}$$

From the first joint and up, the crane can be recognized as the elbow manipulator from (Spong et al., 2005). The angles of this configuration can be found as

$$\begin{aligned} \beta_0 &= \arctan\left(\frac{y_b^0}{x_b^0}\right), \quad \beta_2 = \arctan\left(\frac{\pm\sqrt{1-\delta^2}}{\delta}\right), \\ \beta_1 &= \arctan\left(\frac{z_b^0 - L_0}{\sqrt{(x_b^0)^2 + (y_b^0)^2}}\right) \\ &\quad - \arctan\left(\frac{L_2\sin\beta_2}{L_1 + L_2\cos\beta_2}\right), \end{aligned} \tag{43}$$

where

$$\delta = \frac{(x_b^0)^2 + (y_b^0)^2 + (z_b^0 - L_0)^2 - L_1^2 - L_2^2}{2L_1L_2}. \tag{44}$$

The two separate solutions for β_2 give elbow-down or elbow-up configuration of the manipulator, as the positive or negative square root, respectively. For this example elbow-up is desired, as seen in Fig. 5.

The Jacobian matrix, $\mathbf{J}_\beta$, determines the velocity relationship between the end effector, $\boldsymbol{\xi}$, and the joints, $\dot{\boldsymbol{\beta}} = \begin{bmatrix} \dot{\beta}_0 & \dot{\beta}_1 & \dot{\beta}_2 \end{bmatrix}^T$. The velocity kinematics can be found as

$$\boldsymbol{\xi}_t^b = \begin{bmatrix} \boldsymbol{v}_t^b \\ \boldsymbol{\omega}_t^b \end{bmatrix} = \mathbf{J}_\beta\dot{\boldsymbol{\beta}} \tag{45}$$

where

$$\mathbf{J}_\beta = \begin{bmatrix} \mathbf{J}_v \\ \mathbf{J}_\omega \end{bmatrix} = \begin{bmatrix} \mathbf{J}_{v_1} \ldots \mathbf{J}_{v_n} \\ \mathbf{J}_{\omega_1} \ldots \mathbf{J}_{\omega_n} \end{bmatrix} \tag{46}$$

in which $\mathbf{J}_v$ is the Linear Velocity Jacobian and $\mathbf{J}_\omega$ is the Angular Velocity Jacobian, where both have a column for every link in Table 3 (Spong et al., 2005). For revolute joints, as in this example, the i^{th} column can be found as

$$\begin{bmatrix} \mathbf{J}_{v_i} \\ \mathbf{J}_{\omega_i} \end{bmatrix} = \begin{bmatrix} \mathbf{z}_{i-1} \times (\mathbf{o}_n - \mathbf{o}_{i-1}), \\ \mathbf{z}_{i-1}. \end{bmatrix}, \tag{47}$$

and since the first link in Table 3 is not movable, this is skipped and the Jacobian matrix can be found as

$$\mathbf{J}_\beta = \begin{bmatrix} \mathbf{z}_1^0 \times (\mathbf{o}_4^0 - \mathbf{o}_1^0) & \mathbf{z}_2^0 \times (\mathbf{o}_4^0 - \mathbf{o}_2^0) & \mathbf{z}_3^0 \times (\mathbf{o}_4^0 - \mathbf{o}_3^0) \\ \mathbf{z}_1^0 & \mathbf{z}_2^0 & \mathbf{z}_3^0 \end{bmatrix}, \tag{48}$$

where all vectors can be found from (39) after calculating the transformation matrices for each link.

8. SYSTEM CONTROLLER

The desired position of the TCP, $\boldsymbol{p}_d^n$, can be given by the crane operator, and should be a position that is not affected by the waves. The desired configuration of the TAC should be such that the TCP has the largest freedom of movement in all directions, i.e. in the middle of the workspace, which gives a desired position in the {t}-frame of $\boldsymbol{p}_d^t = [x_d \quad 0 \quad 0]^T$, where x_d can be found by analyzing the workspace area. The crane joints angle can be found by substituting L_2 in (43) and (44) with $L_{2d} = L_2 + x_d$, as $\boldsymbol{p}_d^t$ only has value along the x-axis.

The position of the TAC changed by the disturbances of the sea, $\boldsymbol{o}_t^n$, can be found as

$$\boldsymbol{o}_t^n = \boldsymbol{R}_b^n\boldsymbol{o}_t^b + \boldsymbol{o}_b^n. \tag{49}$$

To compensate for the vessel's motion, the TCP should be moved equally in the opposite direction of the disturbance, thus the positional reference should be a vector from $\boldsymbol{o}_t^n$ to $\boldsymbol{p}_d^n$ in the {t}-frame, found as

$$\boldsymbol{p}_{ref}^t = \boldsymbol{R}_n^t\boldsymbol{p}_{ref}^n, \tag{50}$$

where $\boldsymbol{R}_n^t = (\boldsymbol{R}_t^b)^T(\boldsymbol{R}_b^n)^T$ and $\boldsymbol{p}_{ref}^n = \boldsymbol{p}_d^n - \boldsymbol{o}_t^n$. After checking if $\boldsymbol{p}_{ref}^t$ is inside the workspace, the reference angles, $\boldsymbol{\alpha}_{ref}$, can be found with the use of the IPK function found in Section 3, such that

$$\boldsymbol{\alpha}_{ref} = IPK(\boldsymbol{p}_{ref}^t). \tag{51}$$

The velocity reference can be found by differentiating (50)

$$\mathbf{v}_{ref}^t = \dot{\mathbf{p}}_{ref}^t = \dot{\mathbf{R}}_n^t\mathbf{p}_{ref}^n + \mathbf{R}_n^t\dot{\mathbf{p}}_{ref}^n, \tag{52}$$

where

$$\begin{aligned} \dot{\mathbf{R}}_n^t &= (\dot{\boldsymbol{R}}_t^b)^T(\boldsymbol{R}_b^n)^T + (\boldsymbol{R}_t^b)^T(\dot{\boldsymbol{R}}_b^n)^T \\ &= -(\mathbf{S}(\boldsymbol{\omega}_t^b)(\mathbf{R}_t^b)^T + (\mathbf{R}_t^b)^T\mathbf{S}(\boldsymbol{\omega}_b^n))(\mathbf{R}_b^n)^T \end{aligned} \tag{53}$$

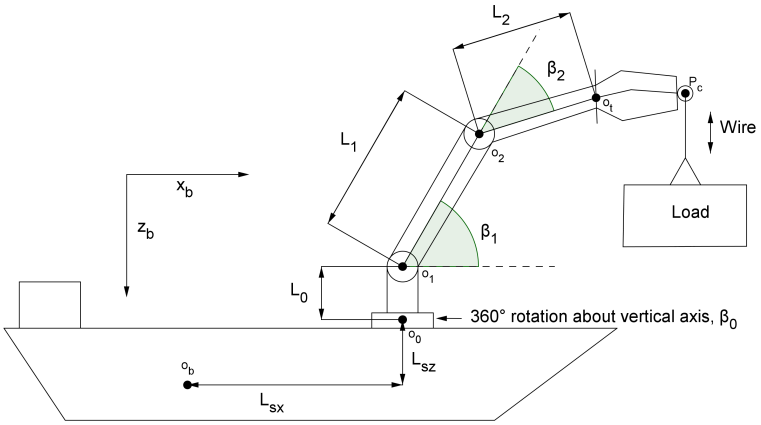

Fig. 5. Ship with full crane system: An elbow manipulator (Spong et al., 2005) and the TAC.

and

$$\begin{aligned}\dot{\mathbf{p}}^n_{ref} &= \dot{\mathbf{R}}^b_t \boldsymbol{p}^t_d + \dot{\mathbf{o}}^b_t - \dot{\mathbf{R}}^n_b \mathbf{o}^b_t - \mathbf{R}^n_b \dot{\mathbf{o}}^b_t - \dot{\mathbf{o}}^n_b \\ &= \mathbf{S}(\boldsymbol{\omega}^b_t)\mathbf{R}^b_t \boldsymbol{p}^t_d - \mathbf{S}(\boldsymbol{\omega}^n_b)\mathbf{R}^n_b \mathbf{o}^b_t + (\mathbf{I} - \mathbf{R}^n_b)\mathbf{v}^b_t - \mathbf{v}^n_b\end{aligned} \tag{54}$$

with

$$\begin{aligned}\mathbf{v}^n_b &= [u \ v \ w]^T, \\ \boldsymbol{\omega}^n_b &= [p \ q \ r]^T.\end{aligned} \tag{55}$$

$\boldsymbol{\omega}^b_t$ and $\mathbf{v}^b_t$ are found from (45). The TCP positional velocity is translated to the joints angular velocity by use of the Jacobian matrix from Section 5,

$$\dot{\boldsymbol{\alpha}}_{ref} = \mathbf{J}^{-1}(\mathbf{p}^t_{ref}, \boldsymbol{\alpha}_{ref})\mathbf{v}^t_{ref}. \tag{56}$$

With error dynamics as $\tilde{\boldsymbol{\alpha}} \equiv \boldsymbol{\alpha}_{ref} - \boldsymbol{\alpha}$ and $\dot{\tilde{\boldsymbol{\alpha}}} \equiv \dot{\boldsymbol{\alpha}}_{ref} - \dot{\boldsymbol{\alpha}}$, the input to the DC-motors, $\mathbf{u}_\alpha = [u_1 \ u_2 \ u_3]$, can be chosen with the use of a PID controller,

$$\mathbf{u}_\alpha = \mathbf{K}_p \tilde{\boldsymbol{\alpha}} + \mathbf{K}_i \int \tilde{\boldsymbol{\alpha}}(t)dt + \mathbf{K}_d \dot{\tilde{\boldsymbol{\alpha}}}, \tag{57}$$

where the controller gains are chosen from regulator tuning.

9. SIMULATION SETUP

The simulation setup consists of the controller described in Section 8, a TAC simulator and a simulated supply vessel with an IMU. An illustration of this is provided in Figure 6.

In the simulator the DC motors used to manipulate $\boldsymbol{\alpha}$ are modeled as the first order system

$$\frac{\boldsymbol{\alpha}}{\mathbf{u}_\alpha}(s) = \frac{K_{DC}}{T_{DC}s + 1}, \tag{58}$$

where values for the motor constants K_{DC} and T_{DC} can be found in Table 4. Inverse Laplace transformation and inserting this equation into (31) yields

$$\dot{\mathbf{p}}^t_c = \mathbf{J}(\mathbf{p}^t_c, \boldsymbol{\alpha})(-\frac{1}{T_{DC}}\boldsymbol{\alpha} + \frac{K_{DC}}{T_{DC}}\mathbf{u}_\alpha), \tag{59}$$

which partially represents the TAC system dynamics. When designing the ship and simulating the IMU data used in this simulator, the MSS toolbox (Fossen, 2011) proved very useful. A supply ship model that takes a controllable wave spectrum as input, and outputs $\boldsymbol{\eta}$ and $\boldsymbol{\nu}$ was created from the MSS toolbox. In the simulations measurement noise was neglected as it is not the focus of this paper, but in (Henriksen and Røine, 2016) it was included in the experiments done on a small-scale prototype of the TAC. Essential parameter values used in the experimental setup can be found in Table 4. The simulator also includes the motion of the full crane, where a path could be generated for the TCP in a pattern such as loading or offloading, and then finding the joint angles through inverse kinematics.

Table 4. Parameter values used in simulations.

Parameter	Value	Unit
l_k	2.00	m
l_a	3.25	m
l_r	7.00	m
l_p	1.25	m
α_{min}	-40	deg
α_{max}	70	deg
T_{DC}	0.2	s
K_{DC}	1	-
K_p	10	-
K_i	60	-
K_d	1	-
L_{sx}	-20.70	m
L_{sz}	3.00	m
L_0	3.00	m
L_1	19.20	m
L_2	9.60	m

10. SIMULATION RESULTS

The conducted experiment used compensation action with only the TAC, with positive results for significant wave height, H_s, up to and including 3.0 meters. This corresponds to sea state 5 (rough sea) (Fossen, 2011). As the focus of this paper is the TAC, the crane is in this simulation placed in a stationary configuration, with

$$\beta_0 = -\frac{\pi}{2} \text{ rad}, \quad \beta_1 == \frac{\pi}{4} \text{ rad}, \quad \text{and } \beta_2 = -\frac{\pi}{4} \text{ rad}, \tag{60}$$

such that the crane points to the starboard side of the ship, with the TAC in parallel with the ship deck, as seen in Fig. 7. The figure also demonstrates the dimensions of the system.

In Fig. 8 the 6 DOF's simulated by the ship simulator can be seen. Fig. 9 shows the how the control loop works with $\mathbf{p}^t_c$ and $\mathbf{p}^t_{ref}$, whereas Fig. 10 shows this in {n}-frame, and compares $\mathbf{p}^n_c$ to the uncompensated TCP position $\mathbf{p}^n_s$. Fig. 11 shows the length position error of the compensation,

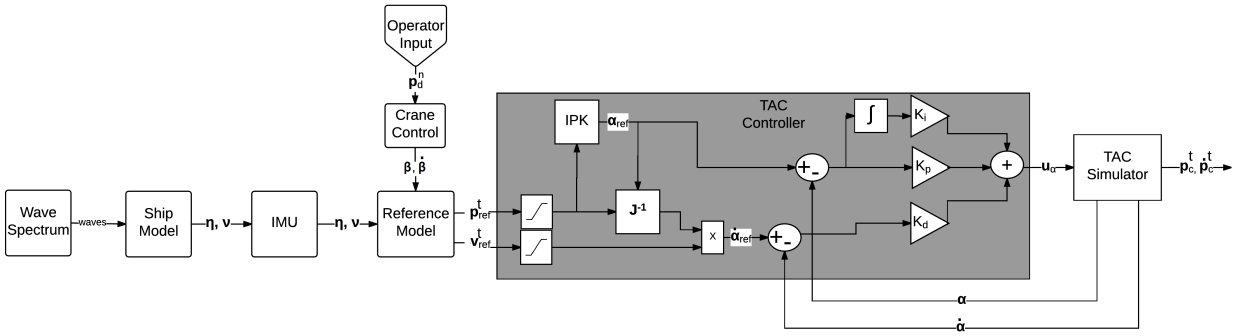

Fig. 6. Block diagram representation of the experimental setup.

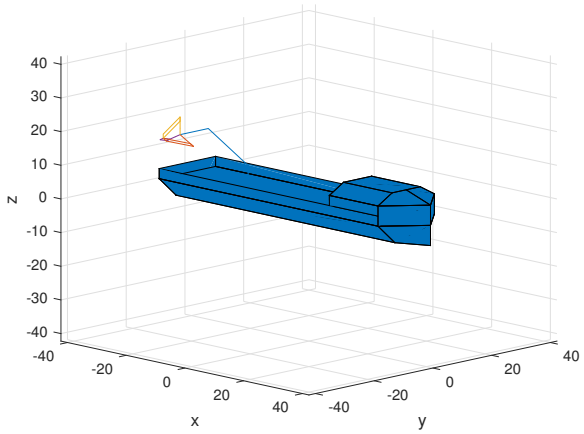

Fig. 7. 3D rendering ship, crane and TAC.

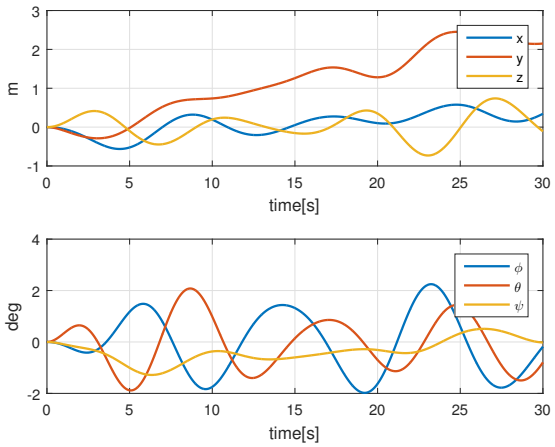

Fig. 8. Simulated vessel position and orientation $\boldsymbol{\eta}$ in {n}-frame.

e_c, compared to the error of the uncompensated case, e_s, calculated as

$$e_c = \|\mathbf{p}_d^n - \mathbf{p}_c^n\|_2, \quad e_s = \|\mathbf{p}_d^n - \mathbf{p}_s^n\|_2. \tag{61}$$

Fig. 12 shows the inputs $\boldsymbol{u}_\alpha$ along with the corresponding $\boldsymbol{\alpha}$. The controller has been tuned such that the position follows the reference closely, as can be seen in Fig. 9.

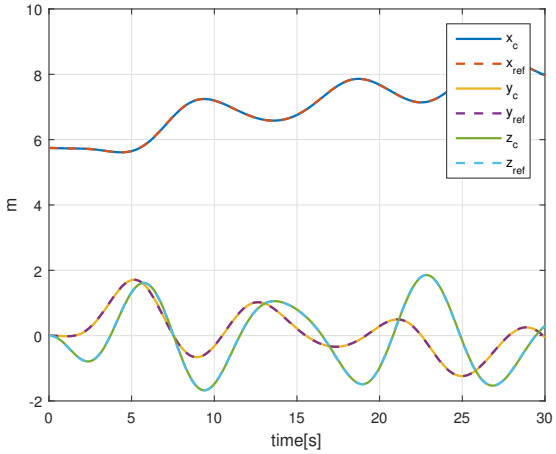

Fig. 9. Simulated TCP position $\boldsymbol{p}_c^t$.

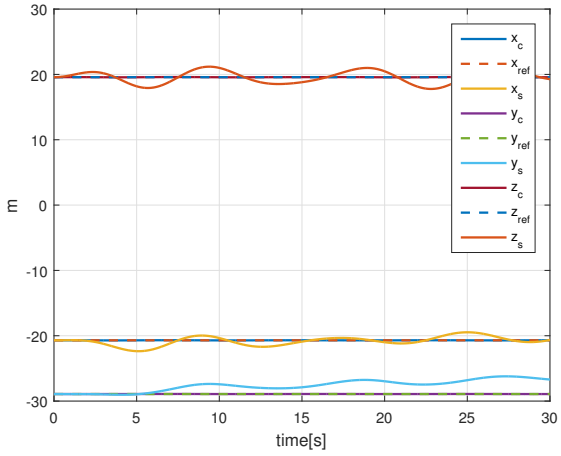

Fig. 10. Simulated TCP position $\boldsymbol{p}_c^n$.

11. DISCUSSION AND CONCLUSION

The goal of this paper is to study how the TAC can be used for motion compensation, and to derive the equations and algorithms needed. Because of the TAC's highly nonlinear nature, this is not a straightforward task, and the solution requires several steps. Controllers for the compensation using merely the TAC has been developed, and shown to be successful in simulations for rough sea. With H_s higher than 3.0 meters the workspace limits were reached,

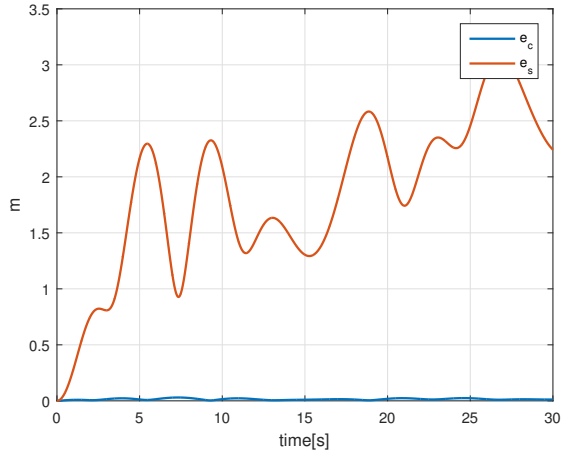

Fig. 11. Error compensated versus uncompensated.

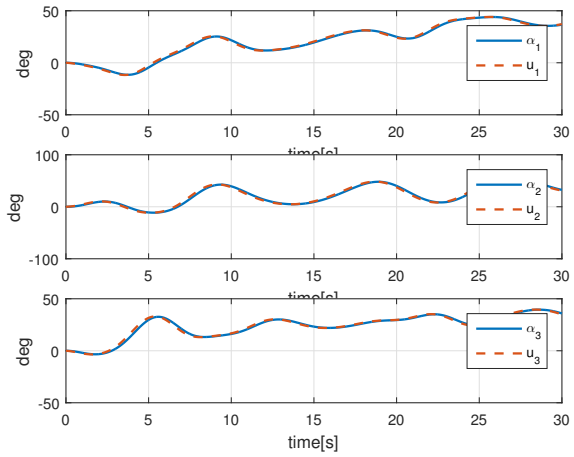

Fig. 12. Simulated angles $\boldsymbol{\alpha}$ and input $\boldsymbol{u}_\alpha$.

which reduces the compensation's efficiency. The TAC provides fast and accurate motion compensation inside its workspace limits. It is reasonable to expect good motion compensation in higher sea if the rest of the crane is also included in the control loop.

The maximum sea state, where the crane can have full mobility, should be determined if it is to be the only compensating force on the cargo. Since the crane's job ultimately is to move its cargo safely to its destination, and not necessarily to keep the TCP still, the workspace requirements might differ and the model must be upgraded to include the suspended load.

REFERENCES

Andrioaia, D., Pascu, M., Mihaila, L., and Obrea, C.F. (2012). Determining the workspace in case of the robots with parallel structure delta 3dof. In *Annals & Proceedings of DAAAM International 2012*, volume 23. DAAAM International.

Clavel, R. (1988). Delta, a fast robot with parallel geometry. In *1988 18th International Symposium on Industrial Robots (ISIR) in Lausanne, Switzerland*, 91–100. Berlin: Springer-Verlag.

Codourey, A. (1988). Dynamic modeling of parallel robots for computed-torque control implementation. *The International Journal of Robotics Research*, 17, 1325–1336.

Coope, I.D. (2000). Reliable computation of the points of intersection of n spheres in $\mathbb{R}^n$. *ANZIAM Journal*, 461–477.

Fang, Y., Wang, P., Sun, N., and Zhang, Y. (2014). Dynamics analysis and nonlinear control of an offshore boom crane. *IEEE Transactions on Industrial Electronics*, 61(1), 414–427.

Fossen, T.I. (2011). *Handbook of Marine Craft Hydrodynamics and Motion Control*. Wiley.

Henriksen, V. and Røine, A. (2016). *Three-Axis Motion Compensated Crane Head Control*. Master's thesis, Norwegian University of Science and Technology.

Johansen, T.A., Fossen, T.I., Sagatun, S.I., and Nielsen, F.G. (2003). Wave synchronizing crane control during water entry in offshore moonpool operations - experimental results. *IEEE Journal of Oceanic Engineering*, 28(4), 720–728.

Küchler, S., Mahl, T., Neupert, J., Schneider, K., and Sawodny, O. (2011). Active control for an offshore crane using prediction of the vessel's motion. *IEEE/ASME Transactions on Mechatronics*, 16(2), 297–309.

Laribi, M.A., Romdhane, L., and Zeghloul, S. (2008). Advanced Synthesis of the DELTA Parallel Robot for a Specified Workspace. *Parallel Manipulators Towards New Applications*, 207–210.

Messineo, S. and Serrano, A. (2009). Offshore crane control based on adaptive external models. *Automatica*, 45(11), 2546 – 2556.

SNAME (1950). The society of naval architects and marine engineers. nomenclature for treating the motion of a submerged body through a fluid. *Technical and Research Bulletin No. 15*.

Spong, M.W., Hutchinson, S., and Vidyasagar, M. (2005). *Robot Modeling and Control*. John Wiley & Sons.

Stan, S.D., Manic, M., Szep, C., and Balan, R. (2011). Performance analysis of 3 dof delta parallel robot. In *2011 4th International Conference on Human System Interactions (HSI)*, 215–220. IEEE.

Williams, R.L. (2015). The delta parallel robot: Kinematics solutions. Internet publication. Www.ohio.edu/people/williar4/html/pdf/DeltaKin.pdf.